Indian Journal of Chemistry
Vol. 61, July 2022, pp. 780-793

Synthesis, characterization, theoretical study and molecular docking studies of some new cobalt(II), chromium(II) and nickel (II) complexes

Sunil Kumar & Mukesh Choudhary*

Department of Chemistry, National Institute of Technology Patna, Patna 800 005, Bihar, India
E-mail: mukesh@nitp.ac.in

Received 19 January 2022; accepted (revised) 07 March 2022

Three transition metal complexes with general formula $[M(L)_2]$ (Co = (**1**), Cr = (**2**) and Ni = (**3**)), were synthesized by treating $CoCl_2/CrCl_3.6H_2O/NiCl_2.6H_2O$ with an ONS-donor Schiff base ligand (HL) derived from the condensation of 3,5-Diiodosalicylaldehyde and 4,4-Dimethyl-3-thiosemicarbazide. The geometry around the centre metal ions was octahedral as revealed by the data collection from spectroscopic studies. The newly synthesized compounds were fully characterized by various physicochemical and spectroscopic methods. DFT calculations were performed on the compounds to get a structure-property relationship. Some global reactivity descriptors like chemical potential (μ), electronegativity (χ), hardness (η) and electrophilicity index (ω) were also evaluated using DFT method. The ADMET prediction analyses have been explored. Molecular dynamics simulations were also studied. Besides this, to find a potential inhibitor for anti-SARS-CoV-2, metal complexes are also assessed through molecular docking and 3-D visualizations of intermolecular interactions against main protease (M^{pro}) of SARS-CoV-2 (PDB ID: 7JKV). The molecular docking calculations of the complex (**1**) into the main protease of SARS-CoV-2 virus (PDB ID: 7JKV) revealed the binding energy of –7.2 kcal/mol with an inhibition constant of 2.529 μM at inhibition binding site of receptor protein. Complex (**2**) with SARS-CoV-2 resulted in the binding energy of –7.8 kcal/mol and the inhibition constant of 5.231 μM. Similarly, complex (**3**) with SARS-CoV-2 (PDB ID: 7JKV) exhibited the binding energy and the inhibition constant of –7.5 kcal/mol and 3.585 μM respectively at inhibition binding site of receptor protein. Overall, *in silico* studies explored the potential role of metal complexes, which would offer new drug candidates against SARS-CoV-2.

Keywords: Transition metal complexes, SARS-CoV-2, molecular docking simulation, DFT calculations

Schiff bases of thiosemicarbazons or semicarbazones coordinate with transition metal ions in tridentate-ONS mode; more diversified binding modes also become possible when an additional coordinating group is present for organometallic and coordination chemistry[1-5]. Throughout history, certain aromatic aldehyde thiosemicarbazones were recognized for their anticancer and antiviral activity[6]. Many thiosemicarbazones have also been tested for antiviral activity. Hamre and his co-workers[7] have reported that *p*-amino benzaldehyde-3-thiosemicarbazone possessed antiviral activity, causing a significant delay in death and survival of a small percentage of chick embryos and mice infected with vaccinia virus. Bauer and Sheffield[8] showed that isatin-β-thiosemicarbazone was capable of protecting mice against infections with lethal doses of the IHD strain of neurotropic vaccinia virus. Rogolino *et al.*[9] have investigated the salicylaldehyde thiosemicarbazone scaffold for inhibition of influenza virus PA endonuclease. Schiff bases have large importance in medicinal and pharmaceutical fields. A lot of papers have been reported in this field and recently several Schiff bases and their complexes have been studied against SARS-CoV-2[10-13]. Furthermore, recent studies have shed a light on molecular docking methodologies as powerful techniques in establishing therapeutic strategies to combat SARS-CoV-2 pandemic. In context to the recent demands, molecular docking and MD simulations approach has been applied for screening of organic molecules and coordination complexes as potent inhibitor of SARS-CoV-2 virus[14-20].

As various molecular docking methodologies are progressing in several directions in the current epidemological context to develop novel therapeutic drugs against SARS-CoV-2 virus, the nature of interaction between 1st row transition metal complexes of cobalt(II), chromium(II) and nickel (II) with main protease of the SARS-CoV-2 would be worthwhile to study. There are no reports indicating the importance of interaction between 1st row transition metal complexes of cobalt(II), chromium(II) and nickel (II) with main protease of the SARS-CoV-2, to the best of our knowledge, so the present study could be of

interest. Herein we report three transition metal complexes with general formula $[M(L)_2]$ (Co = (**1**) , Cr = (**2**) and Ni = (**3**), L= tridentate ONS donor ligand) and its interaction with main protease (M^{pro}) of SARS-CoV-2 (PDB ID:7JKV) are studied by molecular docking methods to find a possible therapeutic drug candidate for SARS-CoV-2 virus. Furthermore, the synthesized complexes showed stable molecular interactions when targeted to the active-site of SARS-CoV-2 M^{pro}. Molecular dynamics simulations were also studied. Besides this, to find a potential inhibitor for anti-SARS-CoV-2, metal complexes is also assessed through molecular docking and 3-D visualizations of intermolecular interactions against main protease (M^{pro}) of SARS-CoV-2 (PDB ID: 7JKV). The molecular docking calculations of the complex (**1**) into the main protease of SARS-CoV-2 virus (PDB ID: 7JKV) revealed the binding energy of -7.2 kcal/mol with an inhibition constant of 2.529 µM at inhibition binding site of receptor protein. Complex (**2**) with SARS-CoV-2 resulted in the binding energy of -7.8 kcal/mol and the inhibition constant of 5.231 µM. Similarly, complex (**3**) with SARS-CoV-2 (PDB ID: 7JKV) exhibited the binding energy and the inhibition constant of -7.5 kcal/mol and 3.585 µM respectively at inhibition binding site of receptor protein. Overall, *in silico* studies explored the potential role of metal complexes, which would offer new drug candidates against SARS-CoV-2.

Results and Discussion

Synthesis

Three transition metal complexes with general formula $[M(L)_2]$ (Co = (**1**) , Cr = (**2**) and Ni = (**3**)), were synthesized by treating $CoCl_2$/ $CrCl_3.6H_2O$/ $NiCl_2.6H_2O$ with an ONS-donor Schiff base ligand (HL) derived from the condensation 3,5-Diiodosalicylaldehyde and 4,4-Dimethyl-3-thiosemicarbazide in equimolar ratio 1:1 in MeOH. Scheme I represents the synthetic routes for Schiff base (HL) and its metal complexes investigated in the present work. They can undergo tautomerization. They are stable in solid state, soluble in water and other common organic solvents.

^{1}H and ^{13}C NMR spectra

The ^{1}H NMR spectrum of Schiff base (HL) and its metal complexes was recorded in DMSO-d_6 solvent and the spectrum data suggests formation of desired products. All of the protons were found to be in their expected regions and numbers, since the complexes contain metal ions in + 2 oxidation state and hence these are paramagnetic in nature. A representative ^{1}H NMR spectrum of Schiff base (HL) is given in Supplementary Information (Figure S1). The azomethine proton (>C=N) of the ligand resonated as a sharp singlet signal at 8.53 ppm. In metal complexes, this signal was shifted 8.57 - 8.62 ppm, indicating the involvement of azomethine group in chelation[21]. Moreover, a singlet signal at 12.97 ppm confirmed the presence of phenolic-OH in the ligand (HL) and was not observed in the studied metal complexes. The multiplet signals in the range of 7.60 - 7.93 ppm with different multiplicity and coupling constants suggested the attribution of the protons of aromatic benzene rings. Furthermore, ^{13}C NMR spectrum of Schiff base (HL) is given in Supplementary Information (Figure S2). The peak assigned to the carbon atom of azomethine group (>C=N) of the ligand was observed at 156.35 ppm. A new additional signal is observed at 146.40 and 179.73 ppm for phenolic carbon and C=S groups, respectively. In case of ^{13}C NMR spectrum of metal complexes, intensity of the signals were very weak and these appear to be merged with the base line, thus we were unable to detect signals as the peaks are merged with noise of the baseline.

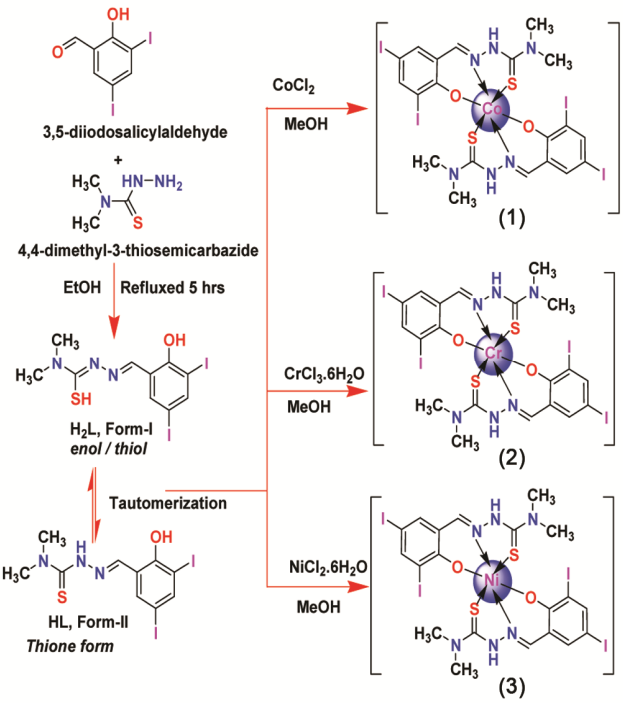

Scheme I — Synthetic route for transition metal complexes investigated in the present work

FT-IR spectral study

The FT-IR spectra of the metal complexes are given in Supplementary Material (Figures S3-S5).The FT-IR spectrum of the complexes are recorded in a KBr pellet, cm^{-1}. Analysis by FT-IR results in the transmittance spectra in the infrared region and register bands or signals. Characteristics peaks in the spectra of the ligand and complexes were considered and compared. In the IR spectrum of the ligand (HL) the highest frequency bands at 3226 cm^{-1} and 3038 cm^{-1} may be assigned to the asymmetric υ(N-H) vibrations, and symmetric υ(N-H) vibrations of the imino and amino groups respectively. These υ(N-H) vibrations has been shifted to higher frequencies (3380-3368 cm^{-1}) in all the complexes at the same positions compared to that of the ligand (HL) indicates that free υ(N-H) vibrations do not participate in coordination. A band appeared at 1222 cm^{-1} for HL due to vibration of the C=S double bond which appeared in the spectra of the complexes and a new band appeared at 1215 cm^{-1} for (**1**), 1313 cm^{-1} for (**2**) and 1310 cm^{-1} for (**3**), indicating that the other coordination is through thiolate sulphur after enolization followed by deprotonating on sulphur. The free ligand (HL) show a sharp intense band at 1645 cm^{-1} assigned to the υ(C=N) of azomethine group. This band has been shifted to higher frequencies appeared at 1662 cm^{-1} for (**1**), 1664 cm^{-1} for (**2**) and 1669 cm^{-1} for (**3**), which indicating the coordination of azomethine nitrogen of ligand to the metal ion. The bands at 712 and 443 cm^{-1} for (**1**), 698 and 483 cm^{-1} for (**2**) and 537 cm^{-1} and 463 cm^{-1} for (**3**) are assigned to M–N and M-O vibrations[22], respectively.

Electronic and fluorescence spectroscopy

Electronic spectra of the metal complexes have been measured in ethanol and the UV-Vis spectra are given in the Supplementary Information (Figure S6). The aromatic bands of the ligand (HL) observed in the range of 330 nm, might be due to benzene π-π* transitions. In addition, the band observed at 370 nm is assigned to the imine π-π* and n-π*transitions. In the spectra of complexes, the bands of azomethine (>C=N) n-π*transition are shifted to longer wavelengths indicating that the imine nitrogen atom is involved in coordination to the metal ion[23]. Each complex exhibited two or three electronic transitions measured and were also observed at different values, thus providing important data on the synthesis of metal complexes. The UV-vis spectra of cobalt(II) complex (**1**) showed two absorption bands at 280 and 400 nm, which are assigned to $^1A_g \rightarrow {}^1E_g$ (n_1) and $^1A_{1g} \rightarrow {}^1B_{2g}$ (n_2) transitions, respectively. Similarly, complex (**2**) shows two absorption bands which are assigned to the $^2B_{1g} \rightarrow {}^2B_{2g}$ (295 nm) and $^2B_{1g} \rightarrow {}^2Eg$ (425). Complex (**3**) showed three strong absorption bands at 275, 300 and 397 nm assigned to $^3A_{2g} \rightarrow {}^3T_{2g}$ (n_1), $^3A_{2g} \rightarrow {}^3T_{1g}$ (F) (n_2) and $^3A_{2g} \rightarrow {}^3T_{1g}$ (P) (n_3), respectively which shows the characteristic peaks of octahedral nickel(II)complexes[24]. Further, the fluorescence spectra of the metal complexes were also recorded in ethanol solution in the range 300-500 nm and spectra are given in Supplementary Information (Figure S6). New complexes (**1**)-(**3**) exhibit fluorescence properties due to presence of functional groups in their structures. Complexes (**1**)-(**3**) showed emission bands at 416-440 nm upon excitation at 340-335 nm (λ_{em} = 340, 425, 440 nm, respectively). One new band was observed at 440 and 438 nm for complex (**1**) and (**3**), which may be caused by the π - π* transitions between the ligand orbitals.The Schiff base ligand (HL) emit in the visible region (530 nm) of spectrum upon the UV-excitation (350 nm). The fluorescence has been caused by the π -π* and n-π* transitions between the ligand orbitals.

Quantum chemical studies of complexes (1)-(3)

The molecular structures of complexes are also obtained computationally. The geometry optimization of metal complexes $[M(L)_2]$ (Co = (**1**), Cr = (**2**) and Ni = (**3**)) were performed at the ωB97X-D/6-311+G** level of theory in vacuum using the Gaussian16 software package[25] and cross-validated using the Spartan 16/18 parallel suite of programs[26]. The dispersion-corrected DFT functional ωB97X-D[27] is chosen to accurately estimate the Vander walls interactions, which are expected to contribute greatly to the stability of the studied complexes. The molecular structure and optimized geometry of the studied metal complexes aredisplayed in Figure 1 and 2, respectively.

The frontier molecular orbitals (FMOs) describing chemical stability of investigated compounds is also interpreted with this analysis and the results are presented in Supplementary Information (Figures S7-S9). The ground state electronic structures of metal(II) complexes are computed features of frontier molecular orbital (FMO) is in terms of energies. The highest occupied molecular orbitals (HOMO) are designated by the π orbitals of proligand whereas the lowest occupied molecular orbitals (LUMO) are

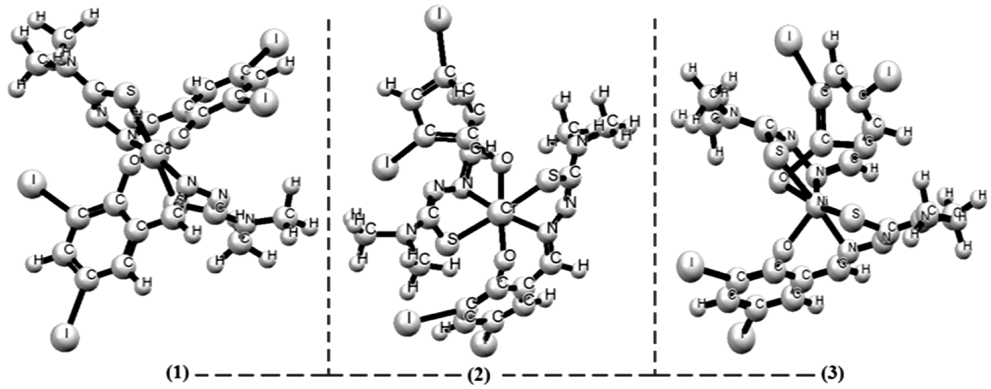

Fig. 1 — Molecular structures of the studied metal (II) complexes (**1**)-(**3**)

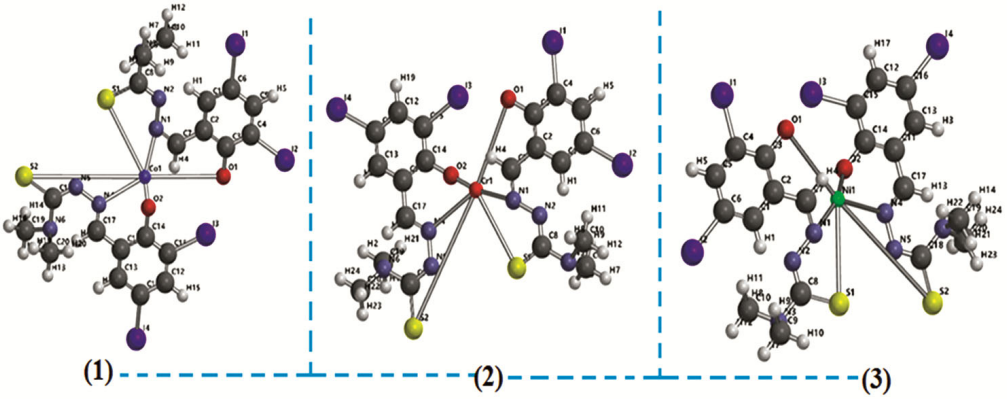

Fig. 2 — Optimized structures of the studied metal (II) complexes (**1**)-(**3**)

assigned by π* ligands. The HOMO exhibits the ability of donating an electron, whereas the LUMO shows that the capabilities of an accepting an electron. The chemical reactivity and stability of the compounds is related to the contribution of frontier orbitals containing HOMO and LUMO location on different parts of the compounds[28]. Furthermore, the differences between the energies of the HOMO and LUMO show different parameters such as activity, stability and excitability. For example, a large HOMO-LUMO energy gap means high excitation energies for many excited states, a good stability and high chemical hardness for the compounds. So, the energy gap of HOMO and LUMO was calculated in order to investigate the stability of the complexes (**1**)-(**3**). The FMOs (HOMO/LUMO and HOMO-1/LUMO+1) energies of the metal complexes were explored and their results are tabulated in Table S1, while their pictorial description of charge densities is displayed in Figures S7 to Figure S9, respectively. The calculated energy gap values of HOMO/LUMO and HOMO-1/LUMO+1 are 1.0 and 2.6 eV for (**1**); 0.5 and 1.8 eV for (**2**); 0.4 and 1.3 eV (**3**). These energy differences (ΔE) between HOMO and LUMO orbitals for complexes are found to be of unequal magnitude. The highest value of ΔE revealed that metal complexes have high chemical stability and low reactivity. Accompanying the energies of FMOs, its analysis also explained the ICT transitions in the metal complexes. The pictograms of charge densities for HOMO/LUMO and HOMO-1 and LUMO+1 are displayed in Figure S7-S9. The charge densities of the LUMO for the metal complexes were located on the metal and the HOMO located on non-metal part. The HOMO and LUMO orbitals are nearly degenerate as shown by a small energy gap and a similar distribution pattern between these two orbitals in the metal complexes.

Furthermore, Global reactivity parameters (GRPs) such as ionization potential (IP), electron affinity (EA), electro negativity (χ), chemical potential (μ), global softness (σ), global hardness (η), and global electrophilicity (ω)using HOMO/LUMO energies[29]. The ionization potential and electron affinity might be utilized to depict the electron gaining and losing capacity of molecules, which interrelated with

HOMO/LUMO energies[30]. In frontier molecular orbitals (FMOs), we have used following **e**quations for global reactivity descriptors[31] as given below:

$$IP = -E_{HOMO} \quad ...(1)$$

$$EA = -E_{LUMO} \quad ...(2)$$

$$X = \frac{[IP + EA]}{2} = -\frac{[E_{LUMO} + E_{HOMO}]}{2} \quad ...(3)$$

$$\eta = \frac{[IP - EA]}{2} = -\frac{[E_{LUMO} - E_{HOMO}]}{2} \quad ...(4)$$

$$\mu = \frac{E_{HOMO} + E_{LUMO}}{2} \quad ...(5)$$

$$\sigma = \frac{1}{2\eta} \quad ...(6)$$

$$\omega = \frac{\mu^2}{2\eta} \quad ...(7)$$

The results obtained from the above equations are tabulated in Table S2 and the results indicate that the values of ionization potential are noticed to be higher than electron affinity values, which disclosed that the studied complex has better capability to accept an electron. The stability as well as reactivity of a chemical system was correlated to chemical potential and global hardness values[32]. The stability had a direct relation with global hardness, whereas it had an inverse relationship to its reactivity[33]. Furthermore, FMO findings explored the HOMO/LUMO bandgap of metal complexes in the range of 0.4-1.0 eV. GRPs explicate that the complexes showed greater ionization potential (IP) (5.9-6.1 eV) than the electron affinity (EA) (5.1-5.6 eV); hence, complexes has greater electron-donating ability. Nevertheless, the metal complexes have also expressed higher values of hardness (η = 0.2-0.5 eV) and a smaller value of softness (σ = 1.0-2.5 eV).

Besides this, molecular electrostatic potentials (MEPs) analyses are done by finding the positive and negative charged electrostatic potential in the compounds. Generally, it presents the interaction energy that result from the interaction between the charge distribution of a molecule and a unit positive charge. The molecular electrostatic potential is related to the electron density and can be used for describing chemical reactivity of compounds[28]. Figure 2 shows 3-D plots of the MEPs (molecular electrostatic potentials) for metal(II) complexes (**1**), (**2**) and (**3**) with iso-value of 0.020 a. u., where negative potential decreases in order of red > orange > yellow > green > blue. According to Figure 3, the higher negative potentials (reddish yellow) are found on oxygen and sulphur atoms of deprotonated Schiff base ligand coordinated to metal (II) ions. There is a visible positive potential (greenish blue) on the surface of metal (II) ions, which indicates its susceptibility towards further nucleophilic substitution reaction. The two nitrogen atoms of ligand show the slight positive potential with slightly greenish blue surface as compared to the rest of the moieties in these complexes. The positive and negative regions can interpret the location of interactions of metal complexes, when they get involved in electrophilic or nucleophilic interactions.

Molecular docking with SARS-CoV-2

There are several Schiff bases and metal(II) complexes which showed good inhibition properties against SARS-CoV-2 . For example, Johnson *et al*. reported[34] that the copper(II) complex of salicylaldehyde benzoyl hydrazone exhibits significantly better inhibitory activity than salicylaldehyde benzoyl hydrazone itself and also found to be relatively non-toxic to mice cells. Adamantanamine hydrochloride is

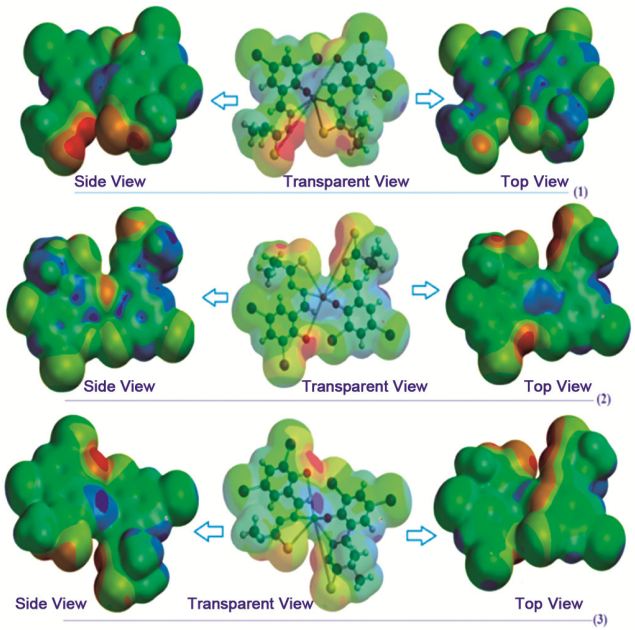

Fig. 3 — The molecular electrostatic potential maps (MEPs) for metal(II) complexes (**1**), (**2**) and (**3**) with iso-value of 0.020 a. u., where negative potential decreases in order of red > orange > yellow > green > blue

Table I — The molecular docking results of the investigated complexes (**1**)-(**3**), and M^{pro} including the binding affinity, inhibition constant and different amino acid residues of SARS-CoV-2M^{pro} that interact with the ligands.

Compounds	Binding affinity (kcal/mol)	Inhibition constant, Ki (μM)	Interacting protein residues		
			H-bond	Electrostatic	Hydrophobic
(**1**)	–7.2	2.529	GLU-166 (3.41Å)	PRO-168 (4.33Å)	GLN-189 (2.27Å), ASN-142 (3.78Å)
(**2**)	–7.8	5.231	ASP-197 (3.54Å)	LYS-137 (4.52Å)	LEU-286 (4.78Å)
(**3**)	–7.5	3.251	GLU-166 (3.40Å)	HIS-163 (5.42Å)	GLN-189 (3.45Å), PRO-168 (5.00Å), THR-190 (3.44Å)

a well-known antiviral drug which a mutation makes influenza virus as amantadine (AdNH2) resistant so a new formalism with copper(II) adamantanamines was found to be effective[35].Very recently, Andreou *et al*.[36] have also studied the role of copper and N-acetylcysteine (NAC) in conjugation with antiviral treatments for SARS-CoV-2. In order to find potent SARS-CoV-2 inhibitor, we have docked complexes with main protease (M^{Pro}) of spike protein (PDB ID: 7JKV) of SARS-COV-2, which is very vital for attaching the virus to its host cell[37]. The stronger binding was predicted between ligand and receptor protein through negative value of binding affinity[38]. As the molecular docking was done to predict the binding affinity and pose of ligand against SARS-COV-2 main protease (PDB ID: 7JKV), we have collected the molecular docking results tabulated in Table I. These include the most important parameters including the binding affinity, inhibition constant and different amino acid residues of M^{pro} that interacts with the complexes. Figure 4 shows the receptor surface of docked conformations for cobalt(II) complex (**1**) inside the M^{pro} , while Figure S10 and S11 displayed receptor surface of docked conformations for chromium(II) complex (**2**) and nickel(II) complex (**3**) inside the M^{pro} with its focused view for interacting residues (PDB ID: 7JKV) with H bond and intermolecular interactions.

Selected amino acid residues between complex (**1**) and SARS-COV-2-M^{pro} (PDB ID: 7JKV) are : GLN-189, PRO-168, GLU-166, ASN-142 for docked complex (**1**); between complex (**2**) and SARS-COV-2-M^{pro} (PDB ID: 7JKV) are :ASP-197, LYS-137, LEU-286 ; between complex (**3**) with SARS-COV-2-M^{pro} (PDB ID: 7JKV) are : GLN-189,HIS-163,GLU-166,PRO-168,THR-190. The molecular docking calculations of the complex (**1**) into the main protease of SARS-CoV-2 virus (PDB ID: 7JKV) revealed the binding energy of -7.2 kcal/mol with an inhibition constant of 2.529 μM at inhibition binding site of receptor protein. Complex (**2**) with SARS-CoV-2

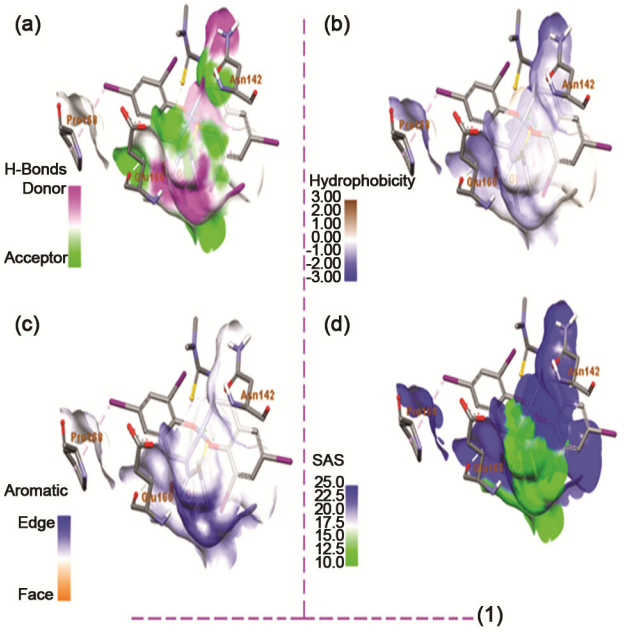

Fig. 4 — Receptor surface of docked conformations for Schiff base cobalt(II) complex (**1**) inside the M^{pro} with its focused view for interacting residues (PDB ID: 7JKV) with H bond and intermolecular interactions; (a) H-bond donor and acceptor meshes represented by pink and light green colors, respectively; (b) hydrophobic pocket represented with blue and brown colors; (c) Aromatic receptor surface represented by blue(Edge) and orange (face) colors; (d) SAS receptor surface represented by blue and green colors, respectively

resulted in the binding energy of -7.8 kcal/mol and the inhibition constant of 5.231 μM. Similarly, complex (**3**) with SARS-CoV-2 (PDB ID: 7JKV) exhibited the binding energy and the inhibition constant of -7.5 kcal/mol and 3.251 μM respectively at inhibition binding site of receptor protein. Overall, *in silico* studies explored the potential role of metal complexes, which would offer new drug candidates against SARS-CoV-2. These binding affinities are reasonably well as compared to recently docked results of anti-SARS-CoV-2 drugs. For instance, the binding affinity of the ligand (HL) and its metal complexes were found to be better than

that of recently docked results of anti-SARS-CoV-2 drugs like chloroquine (-6.293 kcal/mol), hydroxychloroquine (-5.573 kcal/mol) and remdesivir (-6.352 kcal/mol) with SARS-CoV-2 M^{pro} [39]. The binding energies of our complexes was also better than cyclohexanone (-8.72 kcal/mol) and curcumin (-6.9 kcal/mol) as reference compounds[40, 41]. Similar observations were found for other Schiff base metal (II) complexes[42,43].

Interactions with SARS-CoV-2

Apart from the binding affinity and inhibition constant values, it is also very important to visualize the hydrogen bond interactions, and intermolecular interactions between studied metal complexes $[M(L)_2]$ (Co = (**1**) , Cr = (**2**) and Ni = (**3**)] with M^{pro} of the SARS-CoV-2. A representation of docked cobalt (II) complex (**1**) inside the M^{pro} protein (PDB ID: 7JKV) with its focused view for interacting residues along with H-bond and intermolecular interactions are displayed in Figure 5. Figure S12 and Figure S13 indicated the docked complexes inside the M^{pro} (PDB ID: 7JKV) with its focused view for interacting residues around the docked complex. Figure 5 shows the docked Schiff base cobalt (II) complex (**1**) inside the M^{pro}(PDB ID: 7JKV) with its focused view for interacting residues around the docked ligand.

There are some important hydrogen bonds and intermolecular interactions also seen between Schiff base complexes with SARS-CoV-2 M^{pro}. These are summarized as: For complex (**1**), one π-hydrogen bond with a distance of 3.41 Å between NH_2 of GLU-166 residue and π-electrons of ligand (HL) inside the complex (**1**) and M^{pro}; π-anionic electrostatic

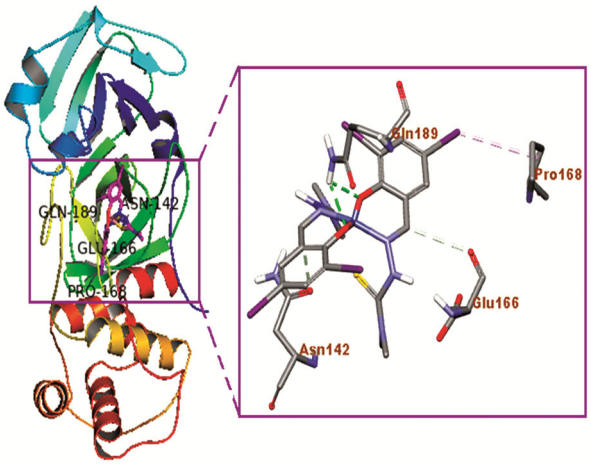

Fig. 5 — The docked Schiff base cobalt (II) complex (**1**) inside the M^{pro} (PDB ID: 7JKV) with its focused view for interacting residues around the docked ligand

interactions between π-orbitals of ligand (HL) and (COO^-) group of anionic PRO-168 residue with distances of 4.33 Å, respectively; two hydrophobic interactions, which are between the π-electrons of ligand and π-electrons of GLN-189 and ASN-142 residues with distances of 2.27 and 3.78 Å, respectively. Similar observations was found for complex (**2**) which are having one π-hydrogen bond with a distance of 3.54 Å between NH_2 of ASP-197 residue and π-electrons of ligand (HL) inside the complex (**2**) and M^{pro}; π-anionic electrostatic interactions between π-orbitals of ligand (HL) and (COO^-) group of anionic LYS-137 residue with distances of 4.52 Å, respectively; one hydrophobic interactions, which are between the π-electrons of ligand and π-electrons of LEU-286 residues with distances of 4.78 Å. In complex nickel(II)(**3**) having one π-hydrogen bond with a distance of 3.40 Å between NH_2 of GLU-166 residue and π-electrons of ligand (HL) inside the complex with M^{pro}; π-anionic electrostatic interactions between π-orbitals of ligand (HL) and (COO^-) group of anionic HIS-163 residue with distances of 5.42 Å, respectively; three hydrophobic interactions, which are between the π-electrons of ligand and π-electrons of GLN-189, PRO-168, THR-190 residues with distances of 3.45, 5.00, 3.44 Å, respectively. Hence, ligand (HL) and its metal complexes cobalt(II) (**1**), chromium(II) (**2**), nickel(II) (**3**) with SARS-COV-2 M^{pro} (PDB ID:7JKV) was stabilized, and ligand and its metal complexes were fitted within the substrate binding packet of SARS-COV-2 main protease (PDB ID: 7JKV) having different binding modes, hydrogen bond interactions, and hydrophobic interactions which are represented in Table I.

Furthermore, H-bond is considered as a significant factor for RNA structure in biological system and H-bond with less than 2.3 Å increases the binding affinity. Most significant H-bonds of ligand (HL) with GLU-166, and chromium (II) (**2**) complex with ASP-197 of amino acid residues of protein in a distance 2.01 Å and 3.54 Å, respectively was identified which is closure to standard antiviral drugs[35]. Instead of conventional hydrogen bonding between ligand and main protease, the other factors (π-bonding, dipole-dipole interactions, electrostatic interactions and hydrophobic interactions) affect the effectiveness of these compounds against the SARS-CoV-2 virus. Figure 6 indicates the total density surfaces representation for docked Schiff base cobalt(II)

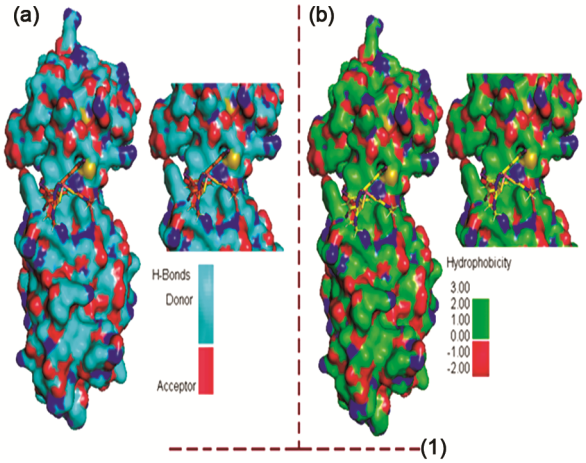

Fig. 6 — The total density surfaces representation for docked Schiff base cobalt(II) complex (**1**) inside the M^{pro} (PDB ID: 7JKV) (a) with hydrogen bond donor and acceptor meshes represented by cyan and red colors, respectively (b) Surface representation of hydrophobic pocket represented with light green and red colors

complex (**1**) inside the M^{pro} (PDB ID: 7JKV) (a) with hydrogen bond donor and acceptor meshes represented by cyan and red colors, respectively (b) Surface representation of hydrophobic pocket represented with light green and red colors.

Figure S14 shows docked Schiff base chromium(II) complex (**2**) inside the M^{pro} (PDB ID: 7JKV) (a) with hydrogen bond donor and acceptor meshes represented by pink and blue colors, respectively (b) Surface representation of hydrophobic pocket represented with deep orange and sky blue colors. Figure S15 presented for docked Schiff base nickel(II) complex (**3**) inside the M^{pro} (PDB ID: 7JKV) (a) with hydrogen bond donor and acceptor meshes represented by deep red and light green colors, respectively (b) Surface representation of hydrophobic pocket represented with light green and blue colors. Figure 7 shows Ligplot for docked Schiff base metal complexes with SARS-CoV-2 M^{pro} (PDB ID: 7JKV). The results obtained from molecular docking indicate that there is H-bond and hydrophobic interactions between of M^{Pro} protein and docked ligand (HL) and its complexes (**1**)-(**3**), which are often considered as crucial factors for potential inhabitation activity.

MD simulation study of complexes (1)-(3)

Furthermore, the protein ligand stable interaction was further confirmed with molecular dynamic simulation for the studied drugs in Schiff base metal complexes. The drug target binding mode of complexes with the SARS-CoV-2 were analysed by

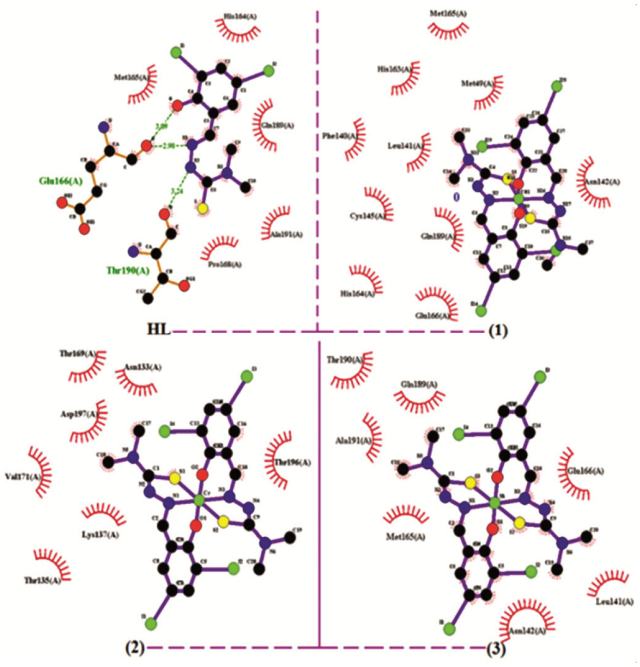

Fig. 7 — Ligplot for docked Schiff base metal complexes with M^{pro} protein (PDB ID: 7JKV)

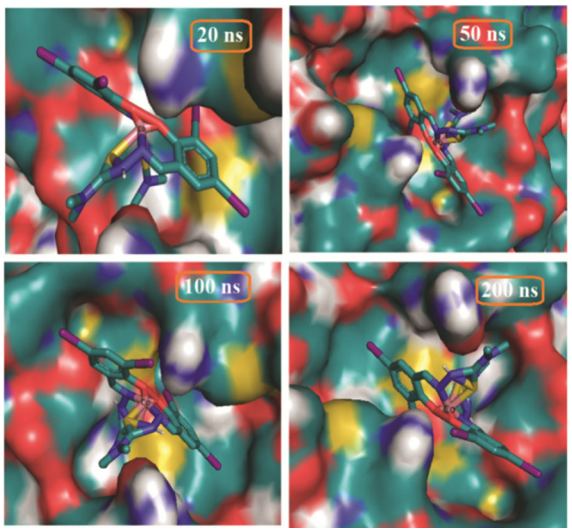

Fig. 8 — Binding mode of Schiff base cobalt (II) complex (**1**) with the SARS-CoV-2 analyzed by generating an average structure from the last 200 ns MD simulation

generating an average structure using 200 ns MD simulation at 20, 50, 100 and 200 ns as reported by Seshan *et al*[44]. Figure 8, Figure 9 and Figure 10 shows the binding mode of studied metal complexes with the SARS-CoV-2 analysed by generating an average structure from the last 200 ns MD simulation. The relationship between docking score and binding affinity may be assumed as the degree of binding of the ligand/metal-target complex with the protein

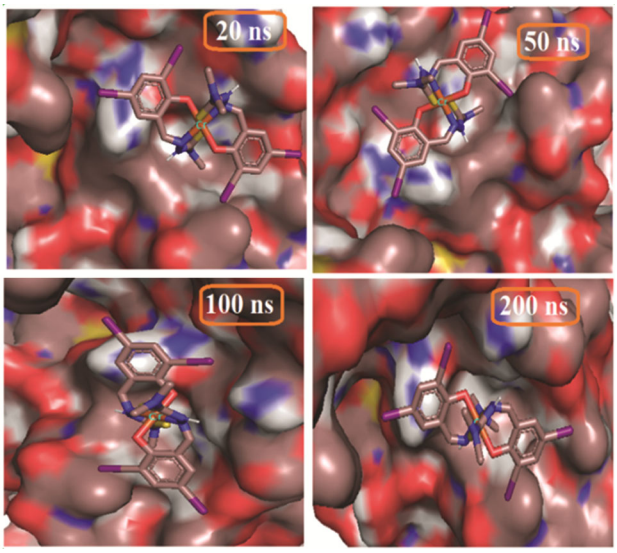

Fig. 9 — Binding mode of Schiff base chromium (II) complex (**2**) with the SARS-CoV-2 analyzed by generating an average structure from the last 200 ns MD simulation

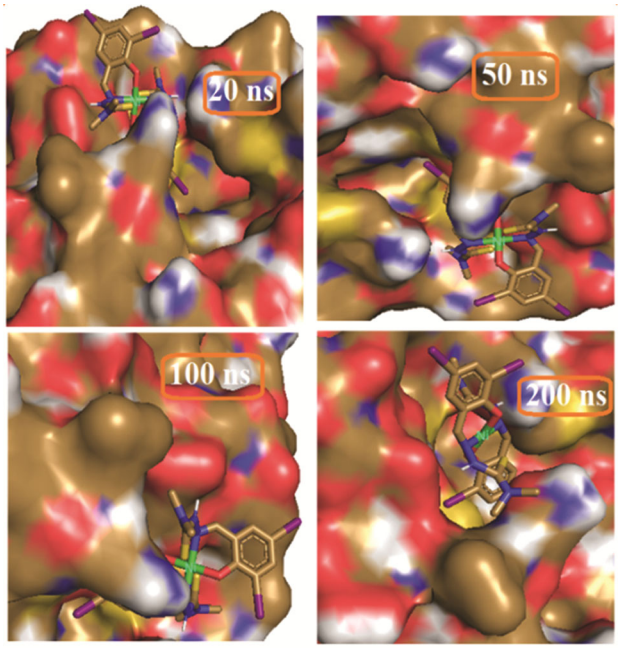

Fig. 10 — Binding mode of Schiff base nickel (II) complex (**1**) with the SARS-CoV-2 analyzed by generating an average structure from the last 200 ns MD simulation

refers to the binding affinity but the docking score is the function used to predict the binding affinity of both ligand/metal and target once it is docked. The ligand occupied in the binding site comprising group of amino acid residues (from Table I) with hydrophobic interactions. Only slight hydrophilic interactions were observed during the course of simulation, which is mainly due to residues GLU-166 and ASP-197 for complexes (**1**)-(**3**) that have contributed for stabilising the hydrogen bond interactions complexes with the SARS-CoV-2, respectively. Our results suggest that the significant residues which stabilize and improve the ligand efficiency into the binding site are mostly due to hydrophobic interactions. The hydrophilic interactions between the ligand and the binding residues are minimal during the course of simulation. The ligand and the protein stability were measured from root mean square deviation (RMSD) value of complexes that was observed for target protein residues. The RMSD value of the redocking is considered for validation of docking of the complexes. The deviation of the structure reversed from the RMSD value was observed minimum and it is evident throughout the course of the simulation with a mean value around 0.25-029 nm. The root mean square fluctuation (RMSF) was used to evaluate the amount of positional fluctuation of each residues of the protein ligand backbone during MD simulation. It was observed that our RMSF value for complexes lies between 0.05 and 0.4 nm with an appropriate average of 0.25-029 nm. Both ligand-receptor and reference receptor complexes have been determined using MD simulations. The ligand interactions with the active site amino acid residues of GLU-166 and ASP-197 for complexes (**1**)-(**3**) were analysed during the 20 ns MD simulations with SARS-CoV-2.

ADMET prediction properties of complexes (1)-(3)

ADMET stands for Absorption, Distribution, Metabolism, Excretion and Toxicity. The predictions of the ADMET properties were investigated and their absorption, distribution, metabolism, excretion and toxic properties[45] for metal complexes (**1**)-(**3**) were evaluated. The physicochemical properties of the complexes were determined by using virtual prediction tool. These compounds were screened through Molinspiration online tool in order to obtain their drug likeness. Molinspiration is used, which facilitates molecular processing and property calculation and the Rule of 5 also helps us to understand ADMET properties of ligands. According to Rule of 5, ligand must carry the following molecular characteristics in order to be considered as a drug molecule: Hydrogen Bond Donor ≤ 5 (OH and NH Groups), Hydrogen Bond Acceptor ≤ 10 (N and O atoms)[46]. Predicted water solubility values (log mol/L) of complexes (**1**)-(**3**) showed comparable water solubility *i.e.*, –4.302 log mol/L, –4.304 log mol/L

and –4.403 log mol/L, respectively. Similarly, all other pharmacokinetic parameters (ADMET) lie between the normal values for all metal (II) complexes with zero violations. Hence, ADMET analysis provides us with in-depth information regarding the development and discovery of the compound as a potential drug. To increase the success rate of complexes towards the higher phase of drug development, we are interested to elucidate its ADMET and toxicity properties. ADMET related pharmacokinetics profile is mentioned in Tables S3 and S4. Pharmacokinetics is the field that studies these four processes of ADME. The pharmacokinetic process of a drug answers whether a drug is able to get into the site of action. The pharmacodynamics process provides the answer of whether or not a drug is able to produce the required pharmacological effect. It is evident that the metal complexes possess better absorption values than standard antibiotics (ampicillin and nystatin). Distribution like BBB (>-1) and CNS (>-2) permeability values are comparable to standard drugs. Their excretion, presented as total clearance, is comparable to ampicillin.

A graphical representation for pharmacokinetics properties for metal complexes (**1**)-(**3**) is shown in Figure 11. In the present study, we have also calculated cheminformatics properties of studied complexes, drug-likeness calculations were calculated from swiss Target Prediction and are summarized in Table S3 and Table S4. It was found that metal(II) complexes have good hydrogen bond donor and acceptor which is consistent with the Lipinski's rule of five. The target was firstly described by its 2-D chemical structures and canonical SMILES along with the bioavailability radar to predict oral bioavailability. Figure 12 shows the bioavailability radar predicted image for ligand (HL) and its complexes (**1**)-(**3**). The bioavailability pie-chart enables a first glance at the drug-likeness of molecules based on well-absorbed and poorly absorbed, their lipophilicity and polarity as described by the n-octanol/water partition coefficient (log P) and the polar surface area (PSA)[47].The pink area represents the optimal range for each property (lipophilicity: XLOGP3 between −0.7 and +5.0, size: MW between 150 and 500 g/mol, polarity: TPSA between 20 and 130 Å^2, solubility: log S not higher than 6, saturation: fraction of carbons in the sp3 hybridization not less than 0.25, and flexibility: no more than 9 rotatable bonds. In this example, the compound is predicted not orally bioavailable, because too flexible and too polar. The metal complexes (**1**)-(**3**) are substrate or inhibitor of iso-enzymes (CYP1A2, CYP2C19, CYP2C9, CYP2D6, CYP3A4) governing important pharmacokinetic behaviors. Inhibition of these isoenzymes is certainly one major cause of pharmacokinetics-related drug-drug interactions.

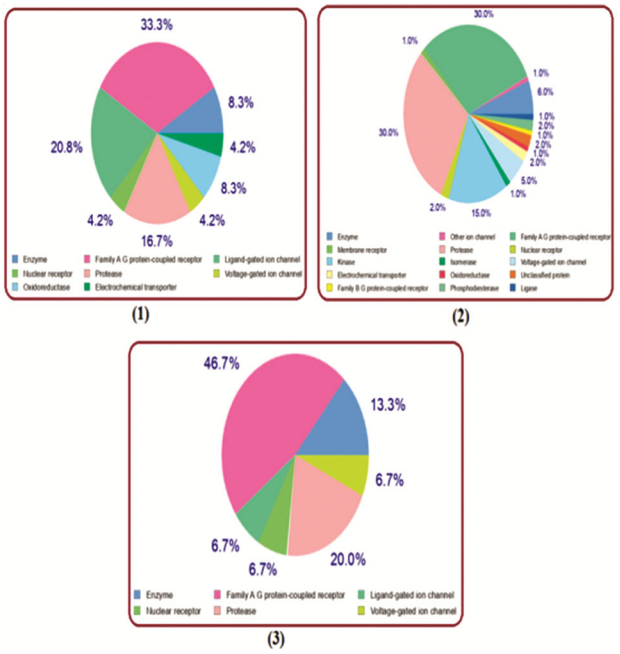

Fig. 11 — ADMET target prediction of the new metal(II) complexes of (**1**)-(**3**)

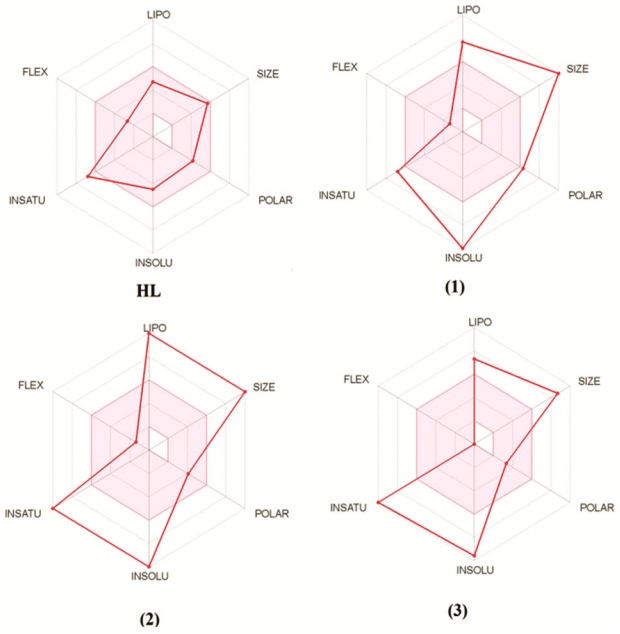

Figure 12 — Bioavailability radar predicted image for complexes (**1**)-(**3**).

Furthermore, Ramachandran plot constructed by using Biovia Discovery Studio 4.1 describing the amino acid residues present in "accepted region" or "unaccepted" region[48]. A better 3D protein model should contain >90% amino acid residues in chosen quadrant of Ramachandran Plot. The Ramachandran backbone shows the statistical distribution of the combinations of the dihedral angles phi (φ) and psi (ψ) plot remains the simplest and sensitive tool[49]. The angle of rotation between the nitrogen and the α-carbon atom is called φ but ψ is the angle of rotation between the α-carbon atom and the carbonyl group. This plot tells about stable conformations of amino acid residues along with favorable and unfavorable regions for amino acid residues. The most favored regions correspond to the core of β-sheet (1st quadrant), core of *α-helix* (right handed cluster at the top of the lower left in the third quadrant) and *α-helix* (left handed in the bottom of the top right in second quadrant). The 4th quadrant occupies the white area, which is 'forbidden' that is sterically disallowed region. There are only three quadrants corresponding to allowed conformations. The Ramachandran diagram satisfies that both the right-handed and the left- handed helices favors the allowed conformations. However, the right-handed helices are energetically more favorable due to less steric clash between the side chains and the backbone. The idealized structures corresponds to φ= -119° and ψ= +113 (parallel β-sheet) and φ=-139, ψ=+135 (antiparallel β-sheet). Antiparallel β sheets are slightly more stable than parallel β sheets.The resulting Ramachandran plot shows that more than 90% of amino acid residues present in the most favored regions (closed curve exhibits cyan color) shown in ligand (HL). Some green bubble and small green triangles cover 9.4% of residues lies in the region of closed curve shown by pink color which are slightly allowed regions. Remaining green bubbles, small green triangles and grey bubbles, small grey triangles lies in the 4th quadrant containing slightly disallowed regions. Figure 13 shows Ramachandran plot representation of phi and psi torsional angles of protein structure for metal (II) complexes (**1**)-(**3**).

Experimental Section

All the solvents used for the synthesis, Cobalt(II) chloride, Chromium(III) chloride hexahydrate, Nickel(II) chloride hexahydrate, 4,4-dimethyl-3-thiosemicarbazide, 3,5-diiodosalicylaldehyde, were obtained from Sigma-Aldrich and were used without further purification. UV-Vis, IR, ^{1}H- and ^{13}C NMR was used to analyse the prepared compounds. Elemental analytical data and quantum chemical calculations were also applied for these purposes. The FT-IR spectra of the compounds were recorded on a Shimadzu IR Affinity-1S Fourier transform infrared spectrophotometer in the range 4000-400 cm^{-1} range using KBr pellets and the electronic spectra of the compounds were taken on a Thermo scientific UV-Vis recording spectrophotometer Evolution-3000 in quartz cells. Melting point was measured on a Boetius micro melting point apparatus. NMR spectra were recorded on a Bruker Ultrashield 500 plus 500 MHz FT-NMR Spectrometer.

DFT calculations

Different quantum chemical parameters obtained from DFT strategies which were estimated to explain the stability and reactivity of the metal complexes. Quantum mechanical methods allow us to calculate different types of energies precisely and interpret various types of complicated interaction between ligand and metal in the formation of complexes. The geometry optimization of metal complexes $[M(L)_2]$ (Co = (**1**) , Cr = (**2**) and Ni = (**3**)) were performed at the ωB97X-D/6-311+G** level of theory in vacuum using the Gaussian16 software package[25] and cross-validated using the Spartan 16/18

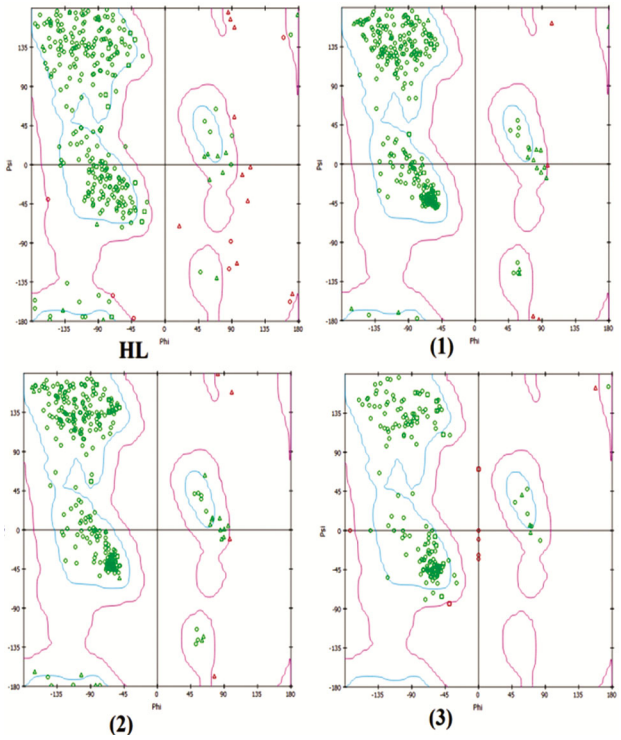

Fig. 13 — Ramachandran plot representation of phi and psi torsional angles of protein structure for metal (II) complexes (**1**)-(**3**).

parallel suite of programs[26]. The dispersion-corrected DFT functional ωB97X-D[27] is chosen to accurately estimate the Vander walls interactions, which are expected to contribute greatly to the stability of the studied complexes.

Molecular docking protocols

All protein docking calculations were performed using open-source AutoDock Tools[50] and AutoDockVina (ADV)[51] programs while docking results were visualized by open-source Discovery Studio visualizer[52]. ADV offers more accuracy in analyzing protein-ligand interactions as compared to Autodock 4.2 where the aforementioned provides more accuracy for a ligand by analyzing more than twenty rotatable bonds[51]. The spike protein of main protease (M^{Pro}) of SARS-CoV-2 was selected for molecular docking and its structure was obtained from the PDB database using (PDB ID: 7JKV) and used as receptor protein[53]. The M^{pro} is a key enzyme of SARS CoV-2 with a molecular mass of 33796.8 Da and plays a pivotal role in the processing of two polyproteins pp1a and pp1ab into 16 NSPS (non-structural proteins)[36]. The Auto Dock GUI program was used to prepare the pdbqt files of the receptor M^{pro} protein, ligand, and metal complexes along with the grid box settings. The grid size boundaries along X, Y, and Z axes were scaled at 30 Å, 30 Å and 30 Å, respectively, with a grid spacing of 0.375 Å to allow proper binding flexibility with a protein molecule. During the re-docking process, we have got the standard value of exhaustiveness number of 24 (default is 8).The output results were written into a configuration file. The receptor protein was treated as a rigid entity whereas ligand and complexes was kept flexible to attain the best fitting confirmation for the receptor complex. On the other hand, Kollman charges, polar hydrogen atoms were also added during the preparation of protein receptor. In addition to this, the water molecules and previously crystalized co-ligand were removed from the receptor molecule through the Auto Dock GUI program[50]. The docking protocol was validated by docking previously crystalized co-ligands with the M^{pro}-7JKV protein. The visualization of results was performed using a free version of Discovery Studio visualizer[52].

Molecular dynamics simulations

The predicted drug target binding mode of metal complexes with the binding mode of SARS-CoV-2 were analyzed by generating an average structure from the last 200 ns MD simulation as reported by Seshan *et al*[44]. MD simulation studies were performed at 200 ns to analyze the steady nature and conformational stability of metal complexes in the physiological environmental conditions, such as temperature, pressures and were embedded with water molecules. The simulation attains plateau with a time step of 2 fs by lead frog Verlet algorithm and MD trajectories were analyzed using the utilities associated with GROMACS package.

ADMET prediction analysis

Online computational approaches were made to predict absorption, distribution, metabolism, excretion and toxicity (ADMET)[54, 55] for metal complexes. The computational prediction of drug could avoid the tremendous cost and time associated with the *in vivo* experiments, and has attracted more and more attention. A large variety of *in silico* methods share the objective of predicting ADMET parameters from molecular structure and their pharmacokinetic and physicochemical parameters[56-58] through free access (http://www.swissadme.ch) that allows to compute physicochemical descriptors as well as to predict ADMET parameters, pharmacokinetic properties, drug-likeness and medicinal chemistry friendliness for one or small molecules.

Synthesis

Synthesis of Schiff base ligand

A tridentate-ONS donor ligand was synthesized as red crystalline products by the refluxing 3,5-diiodosalicylaldehyde (20.0 mmol, 7.478 g) with 4,4-dimethyl-3-thiosemicarbazide (20.0 mmol, 2.383 g) in equimolar ratio 1:1 in MeOH for 4hr.The red crystalline product was obtained, which was filtered, washed with diethyl ether and stored in a desiccator over $CaCl_2$. Colour: Yellowish brown; Yield: 75%; M.p.: > 250°C. FT-IR (KBr/cm^{-1}): 1645 (>C=N); 3226 (**ν**OH). 1306 (C=S), 3038 (C-H), 1648-1564 (C-C) and 3390 (N-H), 831 (-C-I). UV-Vis (DMF) **λ** (nm): 300, 350; $\underline{\boldsymbol{\lambda}}_{max}$ = 370 nm. Fluorescence (MeOH) **λ** (nm): 350,530.^{1}H NMR (500 MHz, DMSO-d_6): δ 12.97 (*s*, 1H, Ar-OH), 11.53 (*s*, 1H, -NH), 8.36 (*S*, 1H, -N=CH), 8.19 (*d*, J=3Hz, 1H, Ar-H), 7.60 (*d*, J= 3Hz, 1H, Ar-H), 3.34 ppm (*m*, 6H,-CH_3). ^{13}C {^{1}H} NMR (DMSO-d_6, 500 MHz): 179.73, 156.35, 146.40, 138.84, 121.10, 88.13, and 40.06 ppm. Anal. Calc. for $C_{10}H_{11}N_3OI_2S$, HL (%): C, 25.58; H, 2.33; N, 8.84. Found (%): C, 25.59; H, 2.34; N, 8.85.

Synthesis of Schiff base complexes (1)-(3)

To a MeOH solution (10 mL) of $CoCl_2$(1.0 mmol, 0.129g)/ $CrCl_3.6H_2O$(1.0 mmol, 0.266 g)/ $NiCl_3.6H_2O$

(1.0 mmol, 0.273 g), a MeOH solution (10 mL) of HL (2.0 mmol, 0.950 g) in the presence of triethylamine (3.0 mmol, 40 µL) as base was added and the reaction mixture was stirred continuously for 5-8 hours at 25°C. The coloured products were collected, washed with MeOH and then washed with diethyl ether, and stored in a desiccator over $CaCl_2$. These complexes gave satisfactory elemental analysis. $[Co(L)_2]$(**1**): Brown color, Yield: 70%, M.p.: >260°C. UV-Vis (MeOH) **λ** (nm): 280,400. Fluorescence (MeOH) **λ** (nm): 340,425.FT-IR data (KBr/cm^{-1}): 3373(phenolic-O), 1662(>C=N), 1215(C=S). Anal. Calcd. for $C_{20}H_{20}CoN_6O_2I_4S_2$ (**1**) , (%): C, 23.85; H, 2.00; N, 8.34. Found (%): C, 23.86; H, 2.01; N, 8.35. $[Cr(L)_2]$(**2**): Red color, Yield: 70%, M.p.: >260°C. UV-Vis (MeOH) **λ** (nm): 295,425. Fluorescence (MeOH) **λ** (nm): 355,450. FT-IR (KBr/cm^{-1}): 3368(phenolic-O), 1664(>C=N), 1313(C=S). Anal. Calcd. for $C_{20}H_{20}CrN_6O_2I_4S_2$ (**2**), (%): C, 24.02; H, 2.02; N, 8.40. Found (%): C, 24.03; H, 2.03; N, 8.41. $[Ni(L)_2]$(**3**): Green color, Yield: 70%, M.p.: >260°C. UV-Vis (MeOH) **λ** (nm): 275,300,397. Fluorescence (MeOH) **λ** (nm): 348,416,438. FT-IR (KBr/cm^{-1}):3380(phenolic-O), 1669(>C=N), 1310(C=S). Anal. Calcd. for $C_{20}H_{20}$ $NiN_6O_2I_4S_2$(**3**), (%): C, 23.86; H, 2.00; N, 8.35. Found (%): C, 23.867; H, 2.01; N, 8.36.

Conclusion

In conclusion, three new metal complexes $[M(L)_2]$ (Co = (**1**) , Cr = (**2**) and Ni = (**3**) , have been synthesized and their anti-SARS-CoV-2 properties were explored. All the newly synthesized complexes were characterized by various physiochemical and spectroscopic methods. Quantum chemical calculations to get insights into the structure-property relationship are presented. ADMET predictions for drug discovery applications are incorporated. Additionally, inspiring by recent developments to find a potential inhibitor for the SARS-CoV-2 virus, we have also performed molecular docking study of complexes to see if our complexes shows an affinity for main protease (M^{pro}) of SARS-CoV-2.

Supplementary Information

Supplementary information is available in the website http://nopr.niscair.res.in/handle/123456789/58776.

Acknowledgments

For computer time, this research used the resources of the Computational Facility at Department of Chemistry, National Institute of Technology Patna, India. The authors must acknowledge to Head, Department of Chemistry, NIT Patna for providing spectral & computational facilities. S. Kumar thankful to NIT Patna, India for research fellowship under TEQIP.

References

1 Petrasheuskaya T V, Kiss M A, Domotor O, Halczbauer T, May N V, Spengler G, Kincses A, Gasparovic A C, Frank E & Enyedy E A, *New J Chem,* 44 (2020) 12154.

2 Ramachandran E, Kalaivani P, Prabhakaran R, Rath N P, Brinda S, Poornima P, Padma V V & Natarajan K, *Metallomics,* 4 (2012) 218.

3 Kotain A, Kamat V, Naik K, Kokare D G, Kumara K, Nemtur K L, Kumbar V, Bhat K & Revankar V K, *Bioorg Chem,* 112 (2021) 104962.

4 Lobana T S, Kumari P, Castineiras A & Butcher R J, *Eur J Inorg Chem,* 2013 (2013) 3557.

5 Bal T R, Anand B, Yogeeswari P & Sriram D, *Bioorg Med Chem Lett,* 15 (2005) 4451.

6 Prescott B & Li C P, *J Med Chem,* 7 (1964) 383.

7 Hamre D, Brownlee K A & Donovick R, *J Immunology,* 67 (1951) 305.

8 Bauer D J & Sheffield F W, *Nature,* 184 (1959) 1496.

9 Rogolino D, Bacchi A, Luca L D, Rispoli G, Sechi M, Stevaert A, Naesens L & Carcelli M, *J Biol Inorg Chem,* 7 (2015) 1109.

10 Al-Janabi A S M, Elzupir A O & Yousef T A, *J Mol Struct,* 1228 (2021) Article 129454.

11 El-Gammal O A, Mohamed F Sh, Rezk G N & El-Bindary A A, *J Mol Liq,* 330 (2021) Article 115522.

12 Uddin M N, Amin M S, Rahman M S, Khandaker S, Shumi W, Rahman M A & Rahman S M, *App Organomet Chem,* 35 (2021) e6067.

13 Mir J M, Majid S A & Shalla A H, *Rev Inorg Chem,* 41 (2021) 199.

14 Hussein R K & Elkhair H M, *J Mol Struct,* 1231 (2021) Article 129979.

15 Meyer-Almes F J, *Comput Biol Chem*, 88 (2020) Article 107351.

16 Pal M, Musib D & Roy M, *New J Chem* 45 (2021) 1924.

17 Gao J, Tian Z & Yang X, *Biosci Trends,* 14 *(*2020) 72.

18 Wang M, Cao R, Zhang L, Yang X, Liu J, Xu M, Shi Z, Hu Z, Zhong W & Xiao G, *Cell Res,* 30 (2020) 269.

19 Terbouche C A R, Abdeldjebar H, Lakhdari H, Bachari K, Roisnel T & Hauchard D, *J Mol Struct,* 1222 (2020) Article 128918.

20 Maldonado N & Amo-Ochoa P, *Dalton Trans,* 50 (2021) 2310.

21 Ustinyuk Y A, Chertov V A, Barinov I V, *J Organomet Chem,* 29 (1971) C53.

22 Cao Y, Liu H, Yuan Z & Wei G, *Aust J Chem*, 70 (2017) 608.

23 Beyazit N, Cakmak D & Demetgul C, *Tetrahedron*, 73 (2017) 2774.

24 Patel R N, Kesharwani M K, Singh A, Patel D K & Choudhary M, *Transit Met Chem*, 33 (2008) 733.

25 Frisch M J, Trucks G W, Schlegel H B, Scuseria G E, Robb M A, Cheeseman J R, Scalmani G, Barone V,

Mennucci B & Petersson G A, *Gaussian 16 Rev A03*, (Wallingford, CT) 2016.
26 Lambert H, Mohan N & Lee T C, *Phys Chem Chem Phys*, 21 (2019) 14521.
27 Chai J D & Gordon M H, *Phys Chem Chem Phys*, 10 (2008) 6615.
28 Mohan B, Choudhary M, Bharti S, Jana A, Das N, Muhammad S, Al-Sehemi A G & Kumar S, *J Mol Struct,* 1190 (2019) 54.
29 Parr R G, Szentpaly L V & Liu S, *J Am Chem Soc*, 121 (1999) 1922.
30 Fukui K, *Angew Chem Int Ed,* 21 (1982) 801.
31 Lawal M M, Govender T, Maguire G E M, Kruger H G & Honarparvar B, *Int J Quantum Chem,* 118 (2018) e25497.
32 Sert Y, Sreenivasa S, Doğan H, Mohan N R, Suchetan P A & F Ucun, *Spectrocrim Acta A*, 130 (2014) 96.
33 Murugavel S, Velan V V, Kannan D & Bakthadoss M, *J Mol Struct,* 1108 (2016) 150.
34 Johnson D K, Murphy T B, Rose N J, Goodwin W H & Pickart L, *Inorg Chim Acta*, 67 (1982) 159.
35 Banti C N, Kourkoumelis N, Hatzidimitriou A G, Antoniadou I, Dimou A, Rallis M, Hoffmonn A, Schmidtke M, McGuire K, Busath D, Kolocouris A & Hadjikakou S K, *Polyhedron*, 185 (2020) Article 114590.
36 Andreou A, Trantza S, Filippou D, Sipsas N & Tsiodras S, *In Vivo*, 34 (2020) 1567.
37 Boopathi S, Poma A B & Kolandaivel P, *J Biomol Struct Dyn,* 39 (2021) 3409.
38 Ferreira L G, Santos R N D, Oliva G & Andricolulo A D, *Molecules*, 20 (2015) 13384.
39 Zhang S, Krumberger M, Morris M A, Parrocha C M T, Griffin J H, Kreutzer A & Nowick J S, *ChemRxiv*, 2020.
40 Basu S, Ramaiah S & Anbarasu A, *Biotechnol Genet Eng Rev*, 37 (2021) 64.
41 Basu S, Veeraraghavan B, Ramaiah S & Anbarasu A, *Microb Pathog*, 149 (2020) Article 104546.
42 Bharti M, Muhammad S, Al-Sehemi A G, Bharti S, Kumar S & Choudhary M, *ChemistrySelect*, 6 (2021) 738.
43 Bharti M & Choudhary M, *J Mol Struct,* 1246 (2021) 131246
44 Seshan G, Kanagasabai S, Ananthasri S, Kannappan B, Suvitha A, Jaimohan S M, Kanagaraj S & Kothandn G, *J Biomol Struct Dyn,* 39 (2021) 6987.
45 Snoussi M, Redissi A, Mosbah A, Feo V D, Adnan M, Aouadi K, Alreshidi M, Patel M, Kadr A & Noumi E, *J Biomol Struct Dyn,* 2021.
46 Lipinski C A, *Drug Discov Today Technol*, 1 (2004) 337.
47 Daina A, Michielin O & Zoete V, *Sci Rep*, 7 (2007) Article 42717.
48 Rasheed U, Ilyas U, Zaman S U, Muhammad S A, Afzaal H & Altaf R*, J Appl Bioinforma Comput Biol*, 7 (2018) 1.
49 Ramachandran G N, Ramakrishnan C & Sasisekharan V, *J Mol Biol,* 7 (1963) 95.
50 Morris G M, Huey R, Lindstrom W, Sanner M F, Belew R K, Goodsell D S & Olson A J, *J Comput Chem*, 30 (2009) 2785.
51 Trott O & Olson A J, *J Comput Chem*, 31 (2010) 455.
52 Biovia D S, *Discovery Studio Visualizer*, v17.2.0.16349.2016 (Dassault Systems, San Diego) 2016.
53 Luan X, Shang W, Wang Y, Yin W, Jiang Y, Feng S, Wang Y, Liu M, Zhou R, Zhang Z, Wang F, Cheng W, Gao M, Wang H, Wu W, Tian R, Tian Z, Jin Y, Jhiang H W, Zhang L, Xu H E & Zhang S, *RCSB PDB-7C8U*, 2020.
54 Matin M M, Uzzaman M, Chowdhury S A & Bhuiyan M M H*, J Biomol Struct Dyn,* 40 (2022) 3668.
55 Shivanika C, Kumar S D, Ragunathan V, Tiwari P, Sunitha A & Devi B P, *J Biomol Struct Dyn,* 40 (2022) 585.
56 Dahlin J L, Inglese J & Walters M A, *Nat Rev Drug Discov,* 14 (2015) 279.
57 Tian S, Wang S J, Li Y, Li D, Xu L & Hou T, *Adv Drug Deliv Rev,* 86 (2015) 2.
58 Daina A & Zoete V, *ChemMedChem,* 11 (2016) 1117.